

SShaDe: a framework for scalable shape deformation via local representations

F. Maggioli¹ , D. Baieri² , Z. Löhner³ , S. Melzi¹ 

¹University of Milano-Bicocca, Italy

²Sapienza - University of Rome, Italy

³University of Bonn, Germany

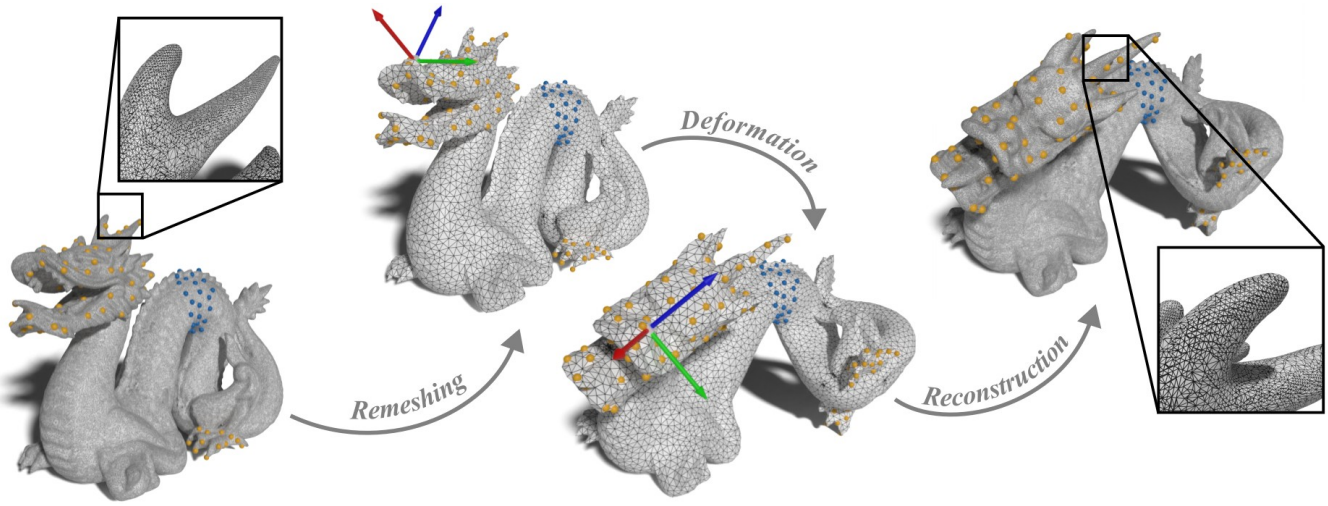


Figure 1: A visual representation of our pipeline on handle-guided deformations. The input mesh (first) is remeshed to a lower resolution (second). The low resolution shape is then deformed (third), and the deformation of the original geometry (fourth) is reconstructed through a representation in a deformation-invariant local reference frame (second and third). Static handles are colored in blue, while dynamic handles are in yellow.

Abstract

With the increase of computational power for the available hardware, the demand for high-resolution data in computer graphics applications increases. Consequently, classical geometry processing techniques based on linear algebra solutions are starting to become obsolete. In this setting, we propose a novel approach for tackling mesh deformation tasks on high-resolution meshes. By reducing the input size with a fast remeshing technique and preserving a consistent representation of the original mesh with local reference frames, we provide a solution that is both scalable and robust. We extensively test our technique and compare it against state-of-the-art methods, proving that our approach can handle meshes with hundreds of thousands of vertices in tens of seconds while still achieving results comparable with the other solutions.

CCS Concepts

• **Computing methodologies** → *Shape modeling*; *Computer graphics*; • **Mathematics of computing** → *Geometric topology*;

1. Introduction and related work

Deforming objects under the preservation of specific properties is one of the cornerstones of computer graphics. One of the most famous and widely used deformation types is as-rigid-as-possible (ARAP) in which the target configuration should be reached while preserving the rigid structure of all surface patches as much as possible [SA07]. Over the years many applications and extensions to this energy have been proposed; from a smoothness prior [LG15] to ARAP regularization terms [HHS*21] and incorporation into neural fields [YSL*22, BML*24]. ARAP is popular because it leads to natural deformations and can be formulated locally; however, optimizing for global optimality is still computationally expensive. As a result deforming high resolution shapes accurately is generally not possible.

A common workaround is to introduce a low-resolution reference graph on which the ARAP energy can be computed efficiently [ZSS97, HLX*20]. This leads to two challenges: 1) how to efficiently and accurately subsample the geometry while preserving the topology of the high-resolution mesh and 2) how to transfer the deformation computed on low-resolution vertices to the high-resolution geometry without introducing artifacts and errors. The first is often a trade-off between efficiency and keeping correspondence information between the high- and low-resolution version. For applications like avatar animation this is not a problem as a single deformation graph is sufficient [HLX*20] but for general shapes retaining this information is not trivial [JSZP20]. However, this information is crucial for the second step where the low-resolution information needs to be transferred on the high-resolution vertices. The deformation of intermediate vertices is going to be a mixture of the deformation of surrounding low-resolution vertices. If not handled correctly, the interpolation might cause artifacts on boundaries and when the surface orientation changes (see Figure 3). Solutions for this problem in multi-resolution settings have been proposed for specific energies [SYBF06, YSL*22] and data types [ZHS*05, YAK*20] but we will present an approach that works independently for any mesh.

This paper presents a novel flexible approach to efficiently compute deformations through a low-resolution mesh and apply them to the original high-resolution shape. We leverage the fast remeshing of [BML*24] which provides a correspondence between the high- and low-resolution versions and perform an accurate reconstruction of geometric details by moving consistent local reference frames. Due to the knowledge of the correspondences this can be done very efficiently. Our experiments show a speed-up of 50x-100x in comparison to other ARAP implementations while keeping comparable metric scores. The method can also be used to tightly align isometrically deformed shapes and perform pose transfer between different classes.

Contributions. Our contributions can be summed up as follows:

- A highly efficient framework for as-rigid-as-possible deformations that works by transferring detailed rigid geometry through local reference frames in a lower resolution.
- An implementation that is 50 to 100 times faster than default ARAP deformation and can be applied to meshes with resolution up to 450k vertices within 10 seconds or less.

- Additionally, the framework can be used to generate tight alignments between isometrically deformed shapes and generate sub-vertex accurate correspondences.

2. Background and notation

Triangular meshes. We discretize a surface as a triangular mesh $\mathcal{M} = (V_{\mathcal{M}}, E_{\mathcal{M}}, T_{\mathcal{M}})$ embedded in \mathbb{R}^3 , where: $V_{\mathcal{M}} \subset \mathbb{R}^3$ is a set of vertices in the 3D space; $T_{\mathcal{M}} \subset V_{\mathcal{M}}^3$ is a set of triangular faces among vertices (invariant under even permutations); $E_{\mathcal{M}} \subset V_{\mathcal{M}}^2$ is a set of edges induced by the triangles (i.e., $(v_i, v_j, v_k) \in T_{\mathcal{M}} \implies (v_i, v_j) \in E_{\mathcal{M}}$).

Manifoldness. Through this paper, we assume our meshes to be 2-manifold. This means that we don't allow a mesh \mathcal{M} to have non-manifold edges (i.e., edges that are incident on three or more triangles), nor non-manifold vertices (i.e., vertices that are incident on two or more fans of triangles). We allow our meshes to have boundaries, that is to have some edges that are incident on a single triangle, but we assume them to be composed by a single connected component.

Deformation. When we refer to a deformation of a mesh $\mathcal{M} = (V_{\mathcal{M}}, E_{\mathcal{M}}, T_{\mathcal{M}})$, we indicate the creation of a second mesh $\mathcal{M}' = (V_{\mathcal{M}'}, E_{\mathcal{M}'}, T_{\mathcal{M}'})$ such that each vertex $v' \in V_{\mathcal{M}'}$ is obtained by altering the 3D position of a corresponding vertex $v \in V_{\mathcal{M}}$, but leaving unchanged the connectivity (i.e., $E_{\mathcal{M}'} = E_{\mathcal{M}}$ and $T_{\mathcal{M}'} = T_{\mathcal{M}}$). When the correspondence between vertices of a mesh \mathcal{M} and its deformation \mathcal{M}' is not implied in the text, we explicitly refer to it as a bijective function $\pi : V_{\mathcal{M}} \rightarrow V_{\mathcal{M}'}$ that preserves the connectivity isomorphism between the two meshes. Namely

$$(v_i, v_j) \in E_{\mathcal{M}} \iff (\pi(v_i), \pi(v_j)) \in E_{\mathcal{M}'}, \quad (1)$$

$$(v_i, v_j, v_k) \in T_{\mathcal{M}} \iff (\pi(v_i), \pi(v_j), \pi(v_k)) \in T_{\mathcal{M}'}. \quad (2)$$

Intrinsic quantities. We use the term *geodesic* as a shorthand for indicating a geodesic shortest path, and the term *geodesic triangle* for indicating a convex region on a surface enclosed by the geodesics connecting three distinct surface points. Scalar functions over the surface are represented as functions $f : V_{\mathcal{M}} \rightarrow \mathbb{R}$ assuming real values at the vertices, while tangent vector fields $F : T_{\mathcal{M}} \rightarrow \mathbb{R}^3$ are defined on triangles. The surface normals are also defined at triangles, and for each triangle t the orientation of its normal n_t is defined by the orientation of its vertices using the right-hand rule. The gradient is an operator $\nabla : \mathcal{F}(\mathcal{M}, \mathbb{R}) \rightarrow \mathcal{F}(\mathcal{M}, \mathbb{R}^3)$ from the space $\mathcal{F}(\mathcal{M}, \mathbb{R})$ of scalar functions over \mathcal{M} to the space $\mathcal{F}(\mathcal{M}, \mathbb{R}^3)$ of vector fields over \mathcal{M} . The gradient $\nabla f(t)$ of a scalar function f at a triangle t returns the tangent vector at t pointing towards the direction of the steepest increase in f .

3. Method

Our method can be summarized by the pipeline in Figure 1. Firstly, we apply a topology-preserving remeshing to obtain a low-resolution version of the original shape while still preserving the overall geometry. We then apply some deformation pipeline to the low-resolution mesh. Finally, we use a robust and conservative local reference frame to reconstruct the original geometry in the deformed pose.

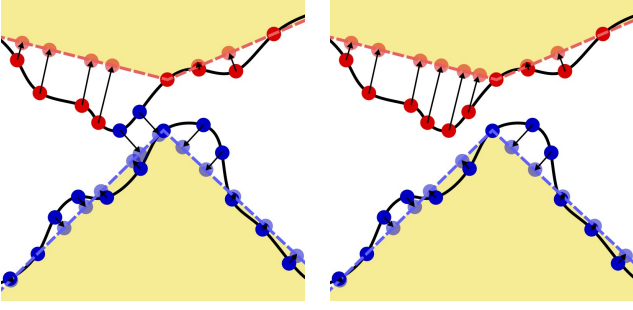


Figure 2: The vertices of a same high-resolution shape (solid) are projected onto the low-resolution representation (dashed, shaded in yellow) with the approach from [MBRM24] (left) and our method (right). The color of the vertices (dark red or dark blue) reveals in which part of the surface they are projected (respectively, light red or light blue).

3.1. Remeshing

For the remeshing step, we rely on the approach proposed by Maggioli *et al.* [MBRM24], as it can efficiently reduce the vertex count by orders of magnitude, while still preserving the original topology and providing robustness guarantees about the preservation of the underlying geometry. Given the original mesh $\mathcal{M} = (V_{\mathcal{M}}, E_{\mathcal{M}}, T_{\mathcal{M}})$ and its remesh $\mathcal{N} = (V_{\mathcal{N}}, E_{\mathcal{N}}, T_{\mathcal{N}})$, the original algorithm also builds an approximately bijective linear mapping $\mathbf{U} \in \mathbb{R}^{V_{\mathcal{N}} \times V_{\mathcal{M}}}$ for upsampling scalar functions over \mathcal{N} to scalar functions over \mathcal{M} . Nonetheless, the map is built using a raw projection of the vertices $V_{\mathcal{M}}$ onto the nearest surface points of \mathcal{N} , an operation who has a $\mathcal{O}(|V_{\mathcal{M}}||T_{\mathcal{N}}|)$ cost. To further reduce this cost, we exploit the fact that each vertex $v \in V_{\mathcal{N}}$ is associated with a Voronoi region $R_v \subset V_{\mathcal{M}}$ onto \mathcal{M} , and that R_v is a topological 2-disk. In this scenario, the original region R_v must be represented by the dual Voronoi area of v on \mathcal{N} , meaning that it is contained inside the triangle fan around v . Thus, for each vertex $v \in V_{\mathcal{N}}$, we project the region R_v onto the nearest surface points of the triangle fan around v . Statistically, the number of triangles incident on a vertex on a manifold mesh is always about 6-7, meaning that the projection operation for a Voronoi region has a $\mathcal{O}(|R_v|)$ cost. By summing across all the regions, we get

$$\sum_{v \in V_{\mathcal{N}}} \mathcal{O}(|R_v|) = \mathcal{O}(|V_{\mathcal{M}}|), \quad (3)$$

achieving a significant improvement in the cost of the projection operation.

This different approach for computing the projection of \mathcal{M} onto \mathcal{N} has the positive side effect of mitigating artifacts and errors in the projection. As shown in the example from Figure 2, the original method proposed in [MBRM24] does not account for regions of the surface that are geodesically far away, but close in the embedding space. Potentially, this situation results in an incorrect mapping of the vertices of \mathcal{M} onto \mathcal{N} . On the other hand, with our approach we ensure that the vertices of each region of \mathcal{M} are mapped into the correct region of \mathcal{N} .

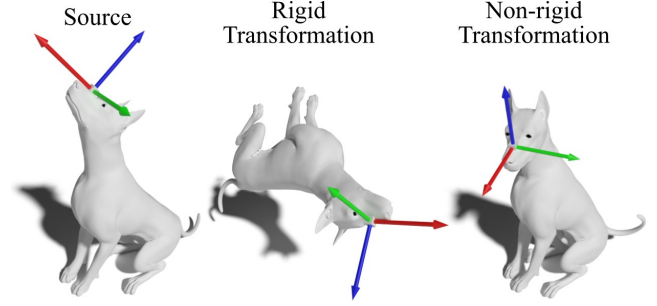


Figure 3: An example of local reference frame at a triangle (left) and how it is affected by a rigid transformation (center) and a non-rigid deformation (right) of the surface. The blue vector is always aligned with the surface normal, the red vector points towards the snout, and the green vector towards the left of the dog's head.

3.2. Local reference frame

Given a mesh $\mathcal{M} = (V_{\mathcal{M}}, E_{\mathcal{M}}, T_{\mathcal{M}})$, the remeshing process produces a mesh $\mathcal{N} = (V_{\mathcal{N}}, E_{\mathcal{N}}, T_{\mathcal{N}})$, which represents \mathcal{M} at a lower resolution, and a mapping $P : V_{\mathcal{M}} \rightarrow T_{\mathcal{N}}$ associating each vertex of \mathcal{M} to the triangle of \mathcal{N} it is projected onto. Since each triangle $t \in T_{\mathcal{N}}$ represents a geodesic triangle t_g onto \mathcal{M} , by building a local reference frame at t , we can completely represent the geometry of t_g in terms of local coordinates in t . Let $\mathcal{N}' = (V_{\mathcal{N}'}, E_{\mathcal{N}'}, T_{\mathcal{N}'})$ a connectivity-preserving deformation of the shape \mathcal{N} (notice that edges and triangles are the same as \mathcal{N}), which may be obtained through an as-rigid-as-possible deformation, manual editing, or any other suitable deformation pipeline. If the local reference frame at triangle t is consistent across deformations, we can use it to reconstruct the global coordinates of the geodesic triangle t_g after the deformation, effectively deforming the original mesh \mathcal{M} into a mesh $\mathcal{M}' = (V_{\mathcal{M}'}, E_{\mathcal{M}'}, T_{\mathcal{M}'})$.

Since we want our local reference frame to be consistent across deformations and variations of pose, we must build it using intrinsic measures and quantities. For this task, we adapt the approach proposed by Melzi *et al.* [MST*19]. In their paper, the authors propose to use the normal vectors and the normalized gradient of some pose-invariant scalar function $f : \mathcal{N} \rightarrow \mathbb{R}$ on the surface (*e.g.*, the Laplacian eigenfunctions) to obtain a local reference frame at the vertices for shape correspondence tasks; the third vector can be easily obtained via a cross product between the other two. A visual representation of how local reference frames are deformed consistently through shapes is shown in Figure 3. As shown in the figure, the three basis vector always represent the same intrinsic directions and the same semantics across the shapes (*e.g.*, the blue vector is always the surface normal and the red vector always points toward the snout). Our setting provides us with a twofold advantage: on one side, we need our local reference frame to be defined over triangles rather than vertices, which is the natural domain for normal vectors and gradient vectors, thus reducing the number of operations to perform and improving numerical stability; additionally, the correspondence between \mathcal{N} and \mathcal{N}' is already known, allowing us to transfer functions accurately by relying on simple functions

Algorithm 1 Deformation transfer via a local reference frame.

```

1: procedure LRFT( $\mathcal{M}, \mathcal{N}, \mathcal{N}', f : V_{\mathcal{N}} \rightarrow \mathbb{R}, P : V_{\mathcal{M}} \rightarrow T_{\mathcal{N}})$ 
2:   for  $t \in T_{\mathcal{N}}$  do
3:      $g_t, g'_t \leftarrow$  gradient of  $f$  at  $t$  on  $\mathcal{N}$  and  $\mathcal{N}'$ , respectively
4:      $n_t, n'_t \leftarrow$  normal at  $t$  on  $\mathcal{N}$  and  $\mathcal{N}'$ , respectively
5:      $w_t \leftarrow g_t \times n_t, \quad w'_t \leftarrow g'_t \times n'_t$ 
6:      $b_t, b'_t \leftarrow$  barycenter of  $t$  in  $\mathcal{N}$  and  $\mathcal{N}'$ , respectively
7:      $\mathbf{L}_t \leftarrow (g_t \ w_t \ n_t), \quad \mathbf{L}'_t \leftarrow (g'_t \ w'_t \ n'_t)$ 
8:   end for
9:    $V_{\mathcal{M}'} \leftarrow \emptyset$ 
10:  for  $v \in V_{\mathcal{M}}$  do
11:     $t \leftarrow P(v)$ 
12:     $v' \leftarrow \mathbf{L}_t^{-1}(v - b_t)$ 
13:     $v' \leftarrow \mathbf{L}'_t v' + b'_t$ 
14:     $V_{\mathcal{M}'} \leftarrow [V_{\mathcal{M}'}, v']$ 
15:  end for
16:  return  $\mathcal{M}' = (V_{\mathcal{M}'}, E_{\mathcal{M}}, T_{\mathcal{M}})$ 
17: end procedure

```

such as the mesh coordinates, avoiding the costly computation of pose-invariant functions. Employing gradient vectors as basis vectors for local reference frames requires caution, as by the Poincaré-Hopf (“Hairy-Ball”) Theorem, not all surface topologies guarantee a non-null tangent vector field everywhere. In cases where we obtain tangent vectors with a very small magnitude at some triangles, we can introduce a second different function $f_2 : \mathcal{N} \rightarrow \mathbb{R}$ on the surface. For each triangle t where $\nabla f(t)$ has a very small magnitude, we can replace the basis vector with $\nabla f_2(t)$. However, as mentioned in [MST*19], in the discrete setting this situation occurs rarely, and we never experienced similar cases in our experiments.

After this process, for each triangle t in the mesh \mathcal{N} , we obtain a matrix \mathbf{L}_t defined as

$$\mathbf{L}_t = (g_t \ w_t \ n_t), \quad (4)$$

where n_t is the normal vector at triangle t , g_t is the gradient vector at t , and $w_t = g_t \times n_t$ is the cross product between the other two. By calling b_t the barycenter of the triangle t , the representation of a vertex $v \in V_{\mathcal{M}}$ in the local reference frame of t is given by

$$v_t = \mathbf{L}_t^{-1}(v - b_t). \quad (5)$$

Similarly, we can build a matrix \mathbf{L}'_t representing the local reference frame of the same triangle t , but in \mathcal{N}' . The reconstruction of the global coordinates for the deformed vertex $v' \in V_{\mathcal{M}'}$ can be obtained through

$$v' = \mathbf{L}'_t v_t + b'_t. \quad (6)$$

The entire procedure is summarized in Algorithm 1, which accepts in input the high-resolution shape \mathcal{M} , its remesh \mathcal{N} , the deformed remesh \mathcal{N}' , a scalar function f over \mathcal{N} , and the projection map of the vertices of \mathcal{M} onto the triangle of \mathcal{N} . The first **for** loop (lines 2-8) computes the local reference frames of all the triangles in both the remeshed shape \mathcal{N} and its deformation \mathcal{N}' . These local reference frames are used in the second **for** loop (lines 10-15) for representing the vertices of \mathcal{M} in local coordinates and deforming them according to \mathcal{N}' .

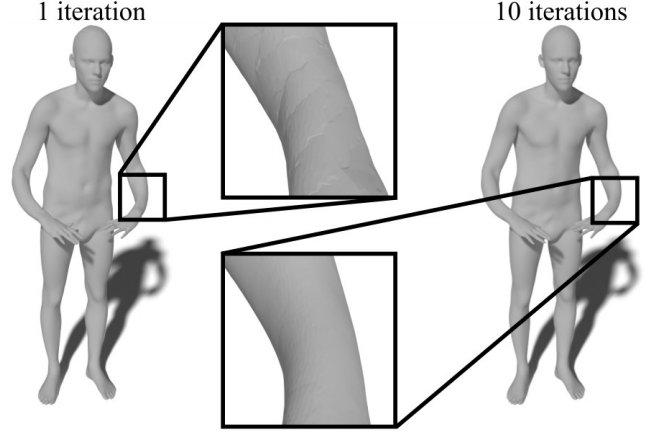


Figure 4: Comparison between the direct application of our approach (left) and the averaging of multiple iterations (right).

3.3. Refinement

The approach we described so far has a major drawback, which is due to the linearity of the local reference frames. Indeed, representing a local reference frame as an affine 3D transformation allows for fast computation, but it also limits the representational power of the deformation. Each geodesic triangle t_g on \mathcal{M} associated with a triangle $t \in T_{\mathcal{N}}$ is deformed according to the same linear transformation induced by the local reference frame. As a result, the deformed mesh at high-resolution presents visual artifacts and lines along the edges of the geodesic triangles, as can be seen in Figure 4. In order to mitigate this effect, we apply multiple iterations of our process using different samplings for computing the low-resolution mesh, resulting in different intrinsic triangulations of \mathcal{M} . Each of these iterations produces a slightly different version of the final mesh \mathcal{M}' , mostly differing only for the placement of the artifact lines. By averaging all these versions of \mathcal{M}' , we obtain a final result where the artifacts are smoothed out, but which still preserves all the details of the original surface. While in our experiments we notice that 5-10 iterations are generally enough, we acknowledge that estimating an optimal number of iterations could be worth of future investigations. We stress that, as each individual iteration is independent, the process can be easily implemented in a multi-threaded environment, averaging all the results at the end and achieving an almost perfect parallelism.

4. Results

For validating the performance of our method, we test its performance on as-rigid-as-possible (ARAP) deformation tasks against state-of-the-art solutions. We also evaluate the pipeline on different types of deformations, for proving its applicability in different contexts. Finally, we show that our approach can be exploited for pose transfer tasks.

Our method is implemented in C++, using as backends the Eigen library for linear algebra routines [GJ*10] and the libigl library for basic geometric operations [JP*18]. All the experiments are per-

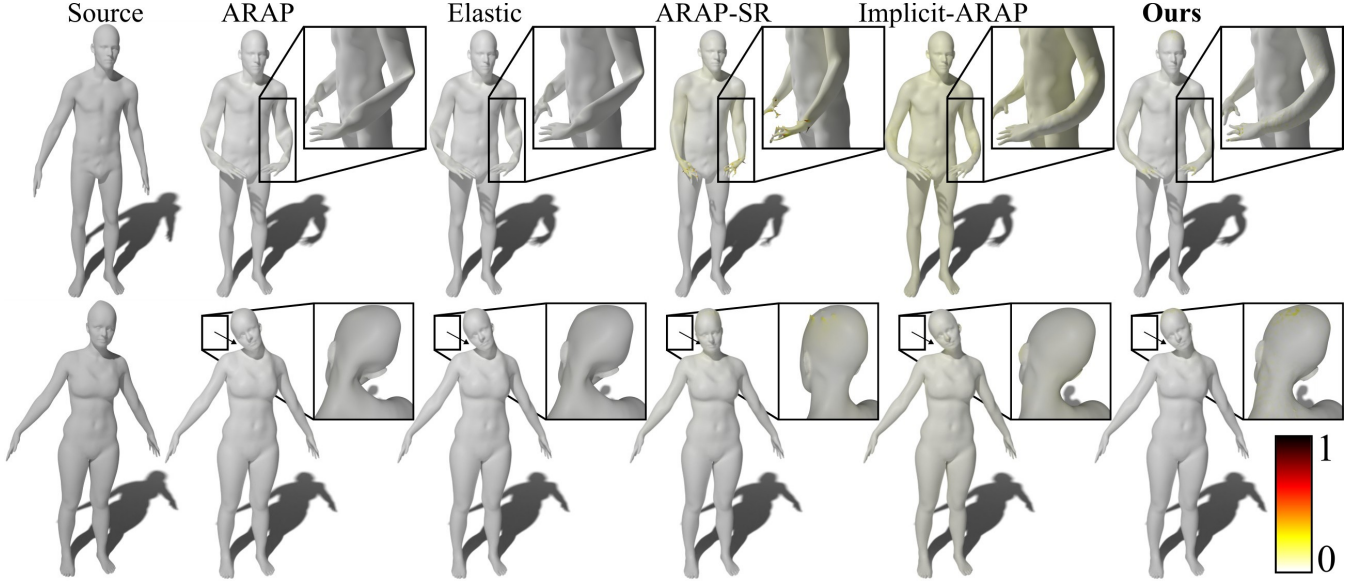


Figure 5: Comparison of our solution with the baseline approaches on sample deformations from the DeFAUST dataset. The close-ups show the deformation artifacts, and the edge error as in Equation (8) is shown as a hot colormap.

formed on a machine equipped with a CPU Intel i7-10700K and 32GB of RAM.

4.1. As-rigid-as-possible deformations

As-rigid-as-possible (ARAP) deformations represent a core task in the field of geometry processing, but most existing solutions are known to suffer from poor scalability to high-resolution meshes. To evaluate the performance of our pipeline in this setting, we compare it against the original ARAP implementation (ARAP) [SA07], the smooth rotations variant (ARAP-SR) [LG15], and the spokes and rims method (Elastic) [CPSS10]. This latter is also the method that we use for deforming our low-resolution shapes, as it is the method that gives the best trade-off between quality and computational cost. Additionally, we also consider the recent work from Baieri *et al.* (Implicit-ARAP) [BML*24], as it provides an efficient and more scalable solutions to previous approaches, while still achieving comparable quality. For our experiments, we use some of the user-defined deformations used in [BML*24], which are based on models from the Stanford’s 3D Scanning Repository (S3D) [sta], as well as our DeFAUST dataset (see Appendix A for an in-depth presentation of the dataset).

For evaluating the results, we follow the approach from [BML*24]. Given the original surface \mathcal{M} and the deformed surface \mathcal{M}' , we consider the relative surface error E_{area} and volume error E_{vol}

$$E_{\text{area}} = \frac{|A_{\mathcal{M}} - A_{\mathcal{M}'}|}{A_{\mathcal{M}}}, \quad E_{\text{vol}} = \frac{|V_{\mathcal{M}} - V_{\mathcal{M}'}|}{V_{\mathcal{M}}}, \quad (7)$$

where A_S and V_S are, respectively, the surface area and the volume of a watertight surface S . We also evaluate the distortion induced on the input geometry by considering the edge length error and

Method	Volume	Area	EL	FA	Time
ARAP	12.41%	0.45%	0.37%	0.517°	7m:15s
Elastic	12.25%	0.45%	0.38%	0.523°	8m:27s
ARAP-SR	11.69%	5.36%	3.39%	5.628°	7m:11s
Implicit-ARAP	0.99%	0.82%	1.06%	1.517°	8m:22s
Ours	2.28%	0.59%	1.28%	2.148°	0m:8s

Table 1: Average errors and execution times for our method and the considered baseline approaches on the DeFAUST dataset. The angle error (FA) is expressed in degrees, while the edge length error (EL), the surface error, and the volume error are in percentage. For each column, the best and second best results are highlighted in light blue and light green, respectively.

the face angle error. Namely, the edge length error is the average difference in length between the same edge before and after the deformation, normalized by the maximum edge length. This can be computed as

$$E_{\text{edge}} = \frac{1}{|E_{\mathcal{M}}|} \sum_{(u,v) \in E_{\mathcal{M}}} \frac{||u-v|| - ||\pi(u) - \pi(v)||}{\max_{e \in E_{\mathcal{M}}} ||e||}, \quad (8)$$

where $\pi : V_{\mathcal{M}} \rightarrow V_{\mathcal{M}'}$ is the point-to-point correspondence between the vertices of the original mesh \mathcal{M} and its deformation \mathcal{M}' . Similarly, the face angle error is the average difference between the same internal angles of the triangles before and after the deformation, which is given by

$$E_{\text{angle}} = \frac{1}{3|T_{\mathcal{M}}|} \sum_{t \in T_{\mathcal{M}}} \sum_{v \in t} \frac{|\angle(v,t) - \angle(\pi(v),t)|}{\angle(v,t)}, \quad (9)$$

where $\angle(v,t)$ is the internal angle of t at vertex v .

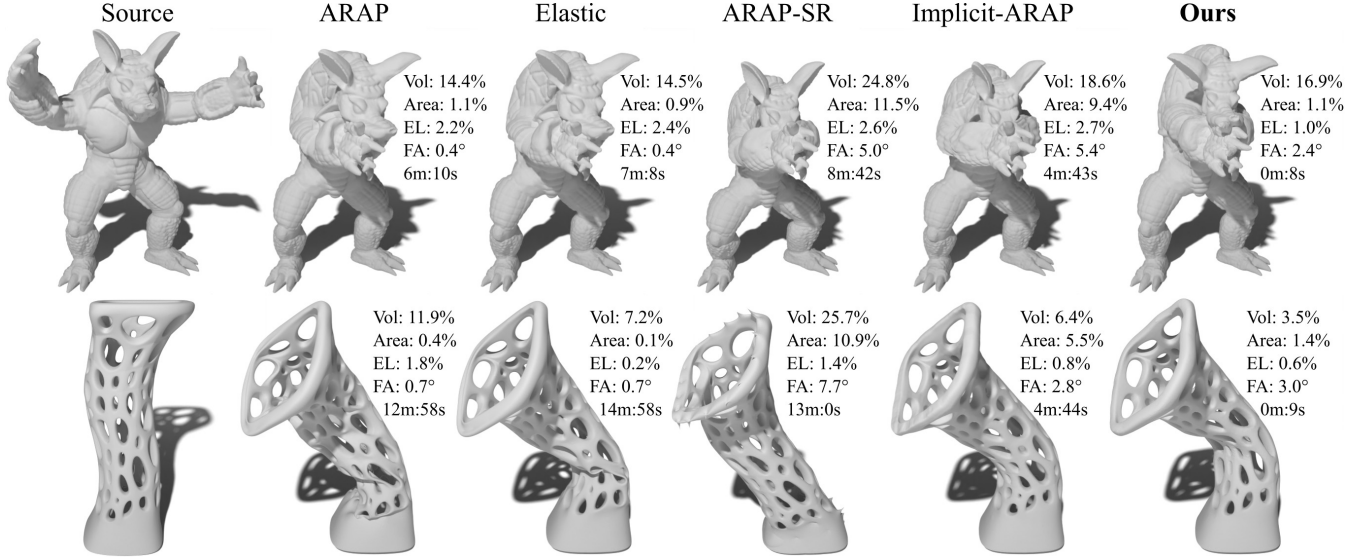


Figure 6: Comparison of our solution with the baseline approaches on some user-defined deformations from [BML*24].

The results of our experiments on the DeFAUST dataset are summarized in Table 1, where we show the error metrics and the runtime averaged across all the 40 high-resolution examples in the dataset. The experiments are run until convergence, with a cutoff of 1000 iterations. For our method, we remesh the original surface to about 6000 vertices, averaging the result across 5 parallel iterations (as discussed in Section 3.3). The configuration parameters of Implicit-ARAP are set to the values suggested by the authors in their paper. From these results, we can see that our approach can achieve comparable results to the other baseline approaches in terms of surface error, edge length error, and face angle error. However, with our method we can compute the deformation at a fraction of the computational cost, obtaining a 50x-60x speedup. Notably, both Implicit-ARAP and our solution achieve significantly better results in terms of volume error. We speculate that this outcome is an intrinsic issue of ARAP and its variants, and that, in fact, the local rigidity constraints only translate to useful volume preservation in a low resolution setting. Clearly, this is not an issue for continuous implicit methods such as Implicit-ARAP, while our method may be seen specifically as a way to account for this issue, since we perform the deformation in a low-resolution representation of the original input. In support to this argument, we highlight that the volume errors for the baselines in the same exact set of experiments on the low-resolution FAUST shapes are much more competitive:

ARAP	Elastic	ARAP-SR
1.28%	1.29%	1.21%

Lastly, the examples in Figure 6 depict a comparison between our method and the other baselines on some user-defined deformations from the original Implicit-ARAP paper. As shown in the figure, with our approach we are able to obtain results that are more visu-

ally plausible with few seconds of computation, instead of several minutes.

4.2. Non-rigid isometric deformations

Our pipeline is not bound to ARAP deformations only: as long as the deformation does not change the number of vertices and their connectivity, our method can be applied to other types of deformations as well. In this regard, we design a set of experiments to test the performance of our pipeline when tackling arbitrary non-rigid isometric deformations. We use the TOSCA dataset [BBK08], which is composed by synthetic meshes representing 9 human and animal subjects in several different poses, including a neutral rest pose. By using the provided correspondence and starting from the rest pose, we reconstruct all the other poses from a low-resolution deformation. Given the rest pose $\mathcal{M} = (V_{\mathcal{M}}, E_{\mathcal{M}}, T_{\mathcal{M}})$ of a subject and another arbitrary pose $\mathcal{M}' = (V_{\mathcal{M}'}, E_{\mathcal{M}'}, T_{\mathcal{M}'})$ of the same subject, we apply the following procedure:

1. we remesh \mathcal{M} to a low-resolution version $\mathcal{N} = (V_{\mathcal{N}}, E_{\mathcal{N}}, T_{\mathcal{N}})$;
2. since $V_{\mathcal{N}}$ is a subset of $V_{\mathcal{M}}$, we use the correspondence provided by the TOSCA dataset to obtain the corresponding vertices $V_{\mathcal{N}'}$ in the target pose;
3. we infer the remesh of the target pose as $\mathcal{N}' = (V_{\mathcal{N}'}, E_{\mathcal{N}'}, T_{\mathcal{N}'})$ using the same connectivity as \mathcal{N} ;
4. using the representation of \mathcal{M} in the local reference frame of the triangles of \mathcal{N} , we transfer the local coordinates onto \mathcal{N}' and reconstruct the deformed mesh \mathcal{M}' .

In Figure 7 we provide visual comparisons between the original meshes from the TOSCA dataset and those reconstructed with our approach. Here we remesh the surfaces to about 6000 vertices and average the result across 10 deformations. We apply this pipeline to the entire TOSCA dataset, comparing the original TOSCA meshes and our reconstruction. We evaluate the results by computing the

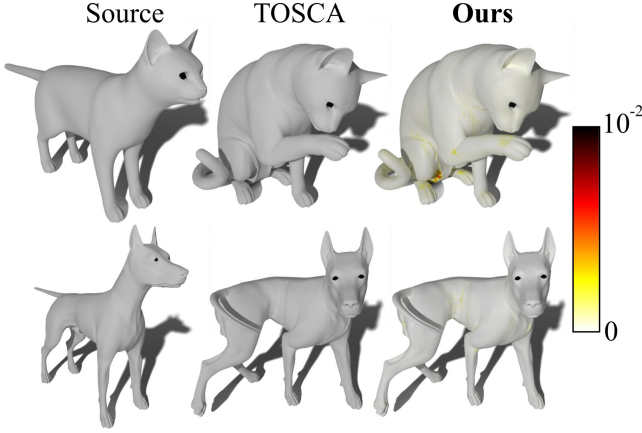


Figure 7: From left to right: a mesh from the TOSCA dataset representing a subject in its rest pose; a mesh from the TOSCA dataset representing the same subject in another pose; the mesh obtained by deforming the rest pose with our pipeline. The Euclidean distance between the deformed mesh and the nearest surface point of the TOSCA mesh is shown as a function on the surface.

Hausdorff distance d_H and the Chamfer distance d_C , which are defined as

$$d_H(\mathcal{X}, \mathcal{Y}) = \max \left(\max_{x \in \mathcal{V}_\mathcal{X}} d(x, \mathcal{Y}), \max_{y \in \mathcal{V}_\mathcal{Y}} d(y, \mathcal{X}) \right), \quad (10)$$

$$d_C(\mathcal{X}, \mathcal{Y}) = \frac{1}{|\mathcal{V}_\mathcal{X}|} \sum_{x \in \mathcal{V}_\mathcal{X}} d^2(x, \mathcal{Y}) + \frac{1}{|\mathcal{V}_\mathcal{Y}|} \sum_{y \in \mathcal{V}_\mathcal{Y}} d^2(y, \mathcal{X}), \quad (11)$$

where $d(v, \mathcal{S})$ represents the Euclidean distance between the point v and the surface \mathcal{S} . For a meaningful comparison, we center all the shapes at the origin of the axes and rescale them to fit inside the unit sphere. Furthermore, we exclude from the experiments the wolf shape for its low vertex count (less than 5000 vertices) and the gorilla shape for its non-manifoldness and high number of connected components. By averaging the results across the entire dataset, we obtain a Hausdorff distance $d_H = 5.66 \cdot 10^{-3}$ and a Chamfer distance $d_C = 3.76 \cdot 10^{-8}$.

4.3. Pose transfer

Another possible use-case scenario for our method is the deformation of a shape into the pose of some other shape. For testing our method in this setting, we manually edit the rest pose of the centaur mesh and the cat mesh from the TOSCA dataset to obtain two new meshes that are semantically similar to the original, but presenting some different features. We notice that the new meshes are in one-to-one correspondence with the original shapes, share with them the same connectivity, and are aligned in the 3D space. Given the rest pose \mathcal{M} from the TOSCA dataset, the edited mesh \mathcal{S} in the rest pose, and a mesh \mathcal{M}' representing the subject \mathcal{M} in a different pose, we want to compute a deformation \mathcal{S}' of \mathcal{S} representing the edited subject in the pose provided by \mathcal{M}' . We remesh the original mesh \mathcal{M} into a low-resolution shape \mathcal{N} , and follow a

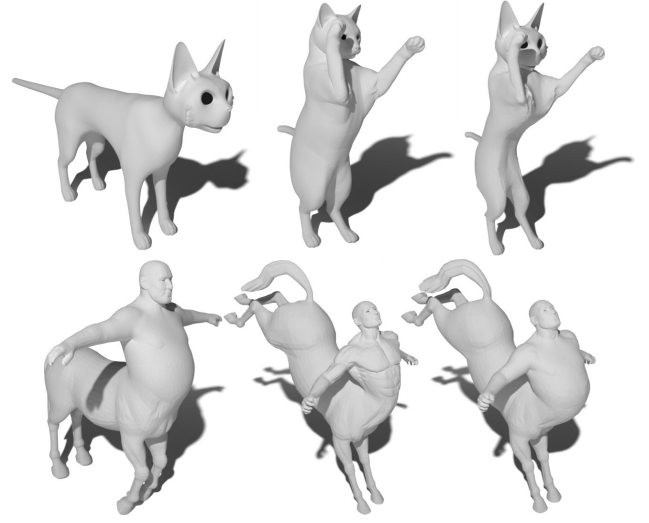


Figure 8: From left to right: a mesh obtained from the rest pose of a TOSCA mesh by manual editing; a mesh from the TOSCA dataset; the manually edited mesh deformed with our method to the pose of the TOSCA mesh.

process similar to the one we describe in Section 4.2. However, instead of computing the local representation of \mathcal{M} onto \mathcal{N} , we use the one-to-one correspondence between \mathcal{M} and \mathcal{S} to compute the local coordinates of the vertices of \mathcal{S} onto the triangles of \mathcal{N} . Then, we reconstruct the mesh \mathcal{S}' representing the edited mesh \mathcal{S} into the target pose provided by \mathcal{M}' .

In Figure 8 we show two examples where we deform our edited centaur and cat meshes from the rest pose to another pose defined by a mesh representing the corresponding original subject. Despite some minor visual artifact, we achieve visually plausible results with about 2 seconds of computation for each examples.

5. Conclusions

We introduced a novel pipeline for tackling efficiently the problem of deforming high-resolution meshes. We exploited a scalable remeshing algorithm to accurately represent a geometry at a lower resolution, and improved the existing approach for mapping vertices at high-resolution onto the low-resolution shape. By taking advantage of the correspondence between a mesh and its deformed counterpart, we implemented an efficient local reference frame at triangles, using it for representing and deforming the original high-resolution geometry. We validated our approach on multiple sets of data, including a novel dataset we introduced for as-rigid-as-possible deformation tasks. Our extensive set of experiments demonstrates the efficiency and efficacy of our approach in multiple settings, including ARAP deformations, non-rigid isometric transformations, and pose transfer tasks.

In the future, we plan exploring other possible applications of our pipeline, like shape matching and other types of mesh editing tasks. We also intend to explore the possibility of softening the re-

quirements of our method, like the assumption of manifoldness and the graph isomorphism constraint between the low-resolution mesh before and after the deformation. Finally, we mean to probe other approaches for representing the high-resolution geometry with local descriptors, eventually increasing their expressive power and enabling more drastic deformations like topological changes.

References

- [BBK08] BRONSTEIN A., BRONSTEIN M., KIMMEL R.: *Numerical Geometry of Non-Rigid Shapes*. Springer, New York, NY, 2008. 6
- [BGS10] BOYÉ S., GUENNEBAUD G., SCHLICK C.: Least squares subdivision surfaces. In *Computer Graphics Forum* (2010), vol. 29, Wiley Online Library, pp. 2021–2028. 9
- [BML*24] BAIERI D., MAGGIOLI F., LÄHNER Z., MELZI S., RODOLÀ E.: Implicit-arap: Efficient handle-guided deformation of high-resolution meshes and neural fields via local patch meshing. *arXiv preprint arXiv:2405.12895* (2024). 2, 5, 6
- [BRLB14] BOGO F., ROMERO J., LOPER M., BLACK M. J.: FAUST: Dataset and evaluation for 3D mesh registration. In *Proceedings IEEE Conf. on Computer Vision and Pattern Recognition (CVPR)* (Piscataway, NJ, USA, June 2014), IEEE. 8
- [CPSS10] CHAO I., PINKALL U., SANAN P., SCHRÖDER P.: A simple geometric model for elastic deformations. *ACM Trans. Graph.* 29, 4 (jul 2010). doi:10.1145/1778765.1778775. 5
- [GJ*10] GUENNEBAUD G., JACOB B., ET AL.: Eigen v3. <http://eigen.tuxfamily.org>, 2010. 4
- [HDD*93] HOPPE H., DEROSE T., DUCHAMP T., McDONALD J., STUETZLE W.: Mesh optimization. In *Proceedings of the 20th annual conference on Computer graphics and interactive techniques* (1993), pp. 19–26. 9
- [HHS*21] HUANG Q., HUANG X., SUN B., ZHANG Z., JIANG J., BAJAJ C.: Arapreg: An as-rigid-as possible regularization loss for learning deformable shape generators. In *2021 IEEE/CVF International Conference on Computer Vision (ICCV)* (2021). 2
- [HLX*20] HABERMANN M., LIU L., XU W., ZOLLHOEFER M., PONS-MOLL G., THEOBALT C.: Real-time deep dynamic characters. *Transactions on Graphics (Proc. of SIGGRAPH)* (2020). 2
- [JP*18] JACOBSON A., PANOZZO D., ET AL.: libigl: A simple C++ geometry processing library, 2018. <https://libigl.github.io/>. 4
- [JSZP20] JIANG Z., SCHNEIDER T., ZORIN D., PANOZZO D.: Bijective projection in a shell. *ACM Transactions on Graphics (TOG)* 39, 6 (2020). 2
- [LG15] LEVI Z., GOTSMAN C.: Smooth rotation enhanced as-rigid-as-possible mesh animation, 2015. doi:10.1109/TVCG.2014.2359463. 2, 5
- [MBRM24] MAGGIOLI F., BAIERI D., RODOLÀ E., MELZI S.: Re-matching: Low-resolution representations for scalable shape correspondence. In *European Conference on Computer Vision* (2024), Springer. 3
- [MST*19] MELZI S., SPEZIALETTI R., TOMBARI F., BRONSTEIN M. M., STEFANO L. D., RODOLÀ E.: Gframes: Gradient-based local reference frame for 3d shape matching. In *Proceedings of the IEEE/CVF Conference on Computer Vision and Pattern Recognition* (2019), pp. 4629–4638. 3, 4
- [SA07] SORKINE O., ALEXA M.: As-rigid-as-possible surface modeling. In *Proceedings of EUROGRAPHICS/ACM SIGGRAPH Symposium on Geometry Processing* (2007), pp. 109–116. 2, 5
- [sta] The stanford 3d scanning repository. <https://graphics.stanford.edu/data/3Dscanrep/>. 5
- [SYBF06] SHI L., YU Y., BELL N., FENG W.-W.: A fast multigrid algorithm for mesh deformation. *ACM Trans. Graph.* 25, 3 (2006). 2

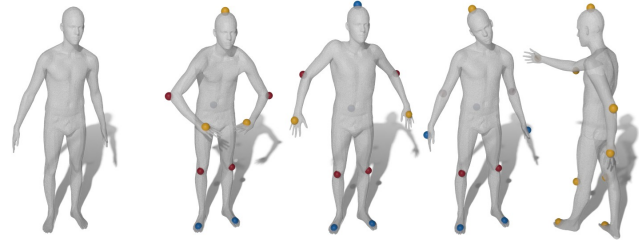


Figure 9: from left to right: the rest pose used in the dataset as the starting position for the deformation; the four target poses used for handle extraction. The landmarks used for the handle generation are color-coded: blue for static handles; yellow for dynamic handles; red for unused handles.

- [YAK*20] YIFAN W., AIGERMAN N., KIM V. G., CHAUDHURI S., SORKINE-HORNUNG O.: Neural cages for detail-preserving 3d deformations. In *CVPR* (2020). 2
- [YBHK21] YANG G., BELONGIE S., HARIHARAN B., KOLTUN V.: Geometry processing with neural fields. In *Advances in Neural Information Processing Systems* (2021), Ranzato M., Beygelzimer A., Dauphin Y., Liang P., Vaughan J. W., (Eds.), vol. 34, Curran Associates, Inc., pp. 22483–22497. URL: https://proceedings.neurips.cc/paper_files/paper/2021/file/bd686fd640be98efaae0091fa301e613-Paper.pdf. 9
- [YSL*22] YUAN Y.-J., SUN Y.-T., LAI Y.-K., MA Y., JIA R., GAO L.: Nerf-editing: geometry editing of neural radiance fields. In *Proceedings of the IEEE/CVF Conference on Computer Vision and Pattern Recognition* (2022), pp. 18353–18364. 2
- [ZHS*05] ZHOU K., HUANG J., SNYDER J., LIU X., BAO H., GUO B., SHUM H.-Y.: Large mesh deformation using the volumetric graph laplacian. *ACM Trans. Graph.* 24, 3 (2005). 2
- [ZSS97] ZORIN D., SCHRÖDER P., SWELDENS W.: Interactive multiresolution mesh editing. *Transactions on Graphics (Proc. of SIGGRAPH)* (1997). 2

Appendix A: DeFAUST dataset

To the best of our knowledge, no dataset exists for quantitative evaluations on deformation methods. For a more exhaustive validation of our method, we introduce the **Deforming FAUST** (DeFAUST) dataset, which is built on top of the well-known FAUST dataset for shape matching [BRLB14]. The FAUST dataset contains 3D scans of real humans in various poses. Among these shapes, 10 subjects in 10 different poses (including a rest pose for each subject) are registered to a template with about 7000 vertices, meaning that all the 100 meshes are in one-to-one correspondence and share the same connectivity.

For each subject, we select the rest pose as the starting pose for the deformation and 4 target poses from which we extract the deformation handles. We also handpick some landmarks which are used for driving the handle extraction. Figure 9 depicts the rest pose and the 4 selected poses, as well as the landmarks that we use for the deformation. Starting from each landmark ℓ on the rest pose \mathcal{M} , we select 30 random vertices in a neighborhood of ℓ , obtaining the

set H_ℓ of handles that drive the deformation of the region represented by the landmark. Then, by using the provided correspondence $\pi : \mathcal{M} \rightarrow \mathcal{M}'$ between \mathcal{M} and another target pose \mathcal{M}' , we select the handles $H'_\ell = \{\pi(v) : v \in H_\ell\}$ on \mathcal{M}' . We then compute the difference

$$\Delta_\ell = \sum_{v \in H_\ell} \|v - \pi(v)\|, \quad (12)$$

and if Δ_ℓ is smaller than some threshold, we mark the positions of the handles H_ℓ as static. Otherwise, we mark them as dynamic handles, using the corresponding positions in H'_ℓ as their target positions. For the last pose on the right of Figure 9 we use more landmark. Differently from the other poses, this pose is not aligned in 3D space with the rest pose, and ARAP methods need more information to solve for a meaningful deformation.

As a result, we obtain a dataset containing 10 different human shapes and 4 sets of deformation handles for each shape. The deformation handles are provided as 3D positions instead of vertex indices, so that they can be used with remeshed and subdivided shapes. Additionally, since we want our dataset to be used also for the evaluation of deformation algorithms on high-resolution meshes, we produce an high-resolution version of the 10 rest pose shapes using the LS3 Loop algorithm [BGS10] to obtain synthetic shapes with an high vertex count. As noted by Yang *et al.* [YBHK21], algorithms for as-rigid-as-possible does not perform well on grid-like triangulations like Marching Cubes meshes or shapes obtained by means of regular subdivisions. For this reason, we apply a step of isotropic remeshing as in [HDD*93] to the subdivided surfaces, obtaining meshes with a vertex count in the range [150k, 200k].